Composite Structures 280 (2022) 114918

Contents lists available at ScienceDirect

Composite Structures

journal homepage: www.elsevier.com/locate/compstruct

Structural and dynamic analysis of a flexible solar array based on shape memory polymer composites

Zhengxian Liu [a], Qifeng Li [a], Xin Lan [b], Wenfeng Bian [c], Liwu Liu [a], Sida Hao [a], Yanju Liu [a], Jinsong Leng [b,*]

[a] Department of Astronautical Science and Mechanics, Harbin Institute of Technology (HIT), Harbin 150001, People's Republic of China
[b] Centre for Composite Materials and Structures, Harbin Institute of Technology (HIT), Harbin 150080, People's Republic of China
[c] Department of Civil Engineering, Harbin Institute of Technology (HIT), Weihai 264209, People's Republic of China

ARTICLE INFO

Keywords:
Dynamic analysis
Flexible solar array
Shape memory polymer composites

ABSTRACT

In recent years, shape memory polymer composites (SMPCs) have been gradually applied to space deployable structures owing to their shape memory characteristics and superior mechanical properties. This study investigated structural and dynamic analysis of an SMPC flexible solar array system (SMPC-FSAS). The SMPC-FSAS was designed to ensure the safety and reliability of the structure. In addition, the modal and swept sine vibration responses of the structure were studied by numerical simulations and experiments. The experimental results were consistent with the numerical simulation predictions, which verified the correctness of the numerical model. Subsequently, a series of dynamic tests verified that SMPC-FSAS has a favorable structural strength and rigidity. Notably, the SMPC-FSAS carried on the SJ-20 geostationary satellite was successfully launched into a geosynchronous orbit, which further verified its safety and reliability. The results of this study are expected to serve the design of ultra-large flexible solar arrays in the future.

1. Introduction

Shape memory polymers (SMPs) are novel functional materials that exhibit shape memory after sensing external stimuli including heat, electric field, magnetic field, solution and light, etc [1–7]. The shape memory mechanism of an SMP is dependent on frozen molecular chains within the polymer, which are gradually activated after external stimulation until the material assumes a specific shape or recovers to its original shape [8–11]. SMPs can be used in aerospace, biomedicine, sensors and many more fields [12–16]. SMPs have the potential to replace the current complex and bulky mechanical deployment mechanism used in space applications. However, SMPs have poor mechanical properties, which affect their use in space deployable structures. These mechanical properties can be effectively improved by introducing reinforcements into SMPs [15,17–22]. This material can achieve three functions: locking before deployment, driving during deployment, and maintaining stiffness after deployment [23].

Traditional solar arrays mostly adopt mechanical deployable structures, which have the disadvantages of complexity, high specific mass and high impact. Deployable structures based on SMPCs realize self-deployment by virtue of their shape memory characteristics, which can effectively reduce the complexity of the mechanical structure. Additionally, owing to the large damping of the deployable structure based on SMPCs, the deployment process is gentle, which has a low impact on the spacecraft [24–27]. There are also some challenges while appreciating the many advantages of SMPCs [15]. SMPCs are limited by the unidirectional deformation of SMPs, and they can't realize automatic folding after deployment. In addition, SMPCs have a limited driving force, they are difficult to drive bulky structures on the ground. However, on-orbit deployment is very easy to implement.

Many studies have been conducted on deployable structures based on SMPCs. Composite Technology Development, Inc(CTD) [28,29] developed a carbon fiber-reinforced epoxy-based hinge and applied it to the solar panel of the DINO Sat satellites. In addition, CTD [30] also designed a new composite lightweight array (CLASP) based on SMPC, which has high packaging efficiency. Liu et al. [31] designed an integrative hinge based on SMPC, which could be used for multi-angle photo systems and solar array deployment in the future. Li et al. [32] studied the truss structure based on SMPC and verified its safety and reliability by numerical simulation and ground mechanics experiments.

* Corresponding author.
E-mail address: lengjs@hit.edu.cn (J. Leng).

https://doi.org/10.1016/j.compstruct.2021.114918
Received 29 April 2021; Received in revised form 13 October 2021; Accepted 28 October 2021
Available online 3 November 2021

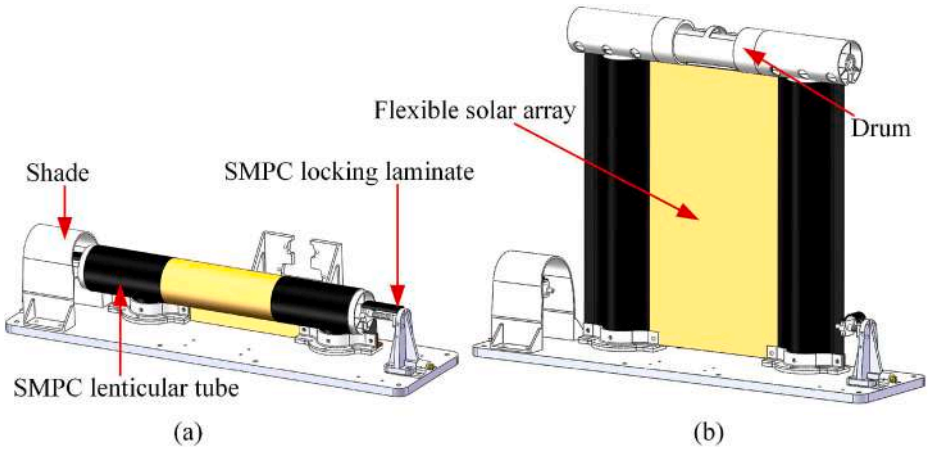

Fig. 1. Structural model diagram:(a) stowed state; (b) deployed state [33].

Table 1
Mass of each part in the SMPC-FSAS.

Parts	SMPC-LLs (g)	SMPC-LTs (g)	Drum (g)	Locking bases (g)	Flexible solar array (g)	Other parts (g)
Mass	2 × 2.8	2 × 25	210	2 × 52	5	1425.4

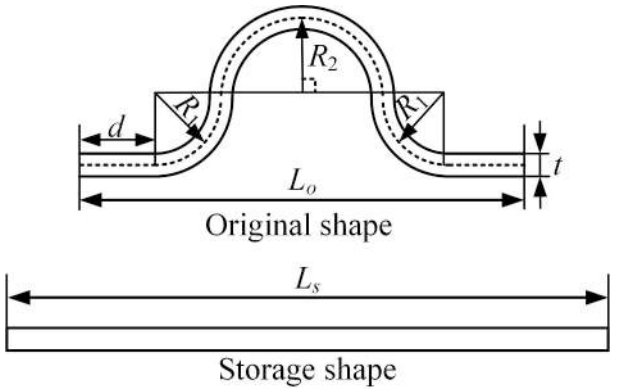

Fig. 2. Original shape and storage shape of the SMPC-LL.

In this study, the structural and dynamic analysis of an SMPC flexible solar array system (SMPC-FSAS) was investigated by considering the dynamic mechanical environment such as vibration, acceleration and shock during launch. The SMPC-FSAS was designed to ensure reliability and security under dynamic environments. The modal and sine frequency sweep analyses of the SMPC-FSAS were carried out by using the software ABAQUS. Subsequently, dynamic environment experiments were performed including vibration, acceleration, and shock experiments. After a series of ground experimental verifications were conducted, the SMPC-FSAS was launched into a geosynchronous orbit.

2. Structural analysis

The SMPC-FSAS was designed to ensure structural resistance to the dynamic environment. The SMPC-FSAS was mainly composed of a locking mechanism and a deployment mechanism. The stowed state and deployed state of the SMPC-FSAS are shown in Fig. 1, where the weight of the SMPC-FSAS was 1.88 kg. The detailed mass of each part in the SMPC-FSAS is listed in Table 1. Previous works have reported the structural performance of SMPC-FASA [33].

The locking and releasing functions of the locking mechanism were realized by the state transform of the SMPC locking laminates (SMPC-LLs). In the locking state, the SMPC-LL was flat (storage state). When the temperature rose to the glass transition temperature (T_g) of the SMPC-LL, the SMPC-LL gradually recovered to the Ω-shape (original state) for the releasing function. The maximum retraction force of the locking mechanism was 18.6 N, in which the spring and SMPC-LT contributed 15 N and 3.6 N respectively. The SMPC-LLs provided a locking force for the SMPC-FSAS at both ends, and the locking force was adjusted to 138 N. The Ω-shape SMPC-LL was selected in the system because the structure was flat in the locked state, which could provide large axial force. After recovery, the retraction of the three arc segments in the middle could provide a large release length. At the same time, the design of the arc could reduce the stress concentration during the deformation process. Fig. 2 shows the original shape and storage shape of the SMPC-LL.

The parameters of the SMPC-LL were calculated as follows:

$$L_o = 2(R_1 + R_2) + 2d \tag{1}$$

$$L_s = \pi(R_1 + R_2) + 2d \tag{2}$$

$$\Delta L = L_o - L_s = (\pi - 2)(R_1 + R_2) \tag{3}$$

where L_o is the original length of the SMPC-LL; L_s is the storage length of the SMPC-LL; ΔL is the release length of the SMPC-LL; R_1 and R_2 are the radius of the arc segment, respectively; d is the straight length. The maximum strain of the arc segment can be described as follows:

$$\varepsilon_1 = \frac{t}{2R_1} \tag{4}$$

$$\varepsilon_2 = \frac{t}{2R_2} \tag{5}$$

where ε_1 and ε_2 denote the maximum strain of the arc segment on both sides and in the middle arc segment of the SMPC-LL, respectively. Substituting Eqs. (4) and (5) into Eq. (3), the equation can be expressed as follows:

$$\frac{1}{\varepsilon_1} + \frac{1}{\varepsilon_2} = \frac{2\Delta L}{(\pi - 2)t} \tag{6}$$

In the design, the straight length d at both ends was the reserved distance for bolt fixation ($d = 5$ mm). The release distance of the SMPC-LL was 4 mm to realize the releasing function. Considering the shape recovery ratio and releasing margin of the SMPC-LL, the release length was designed as 10 mm. In addition, to reduce the probability of damage, the minimum deformation strain of the SMPC-LL was required. According to Eq. (6), this requirement could be met when $R_1 = R_2$. At the same time, to achieve a release length of 10 mm, the arc radius could be determined as 4.38 mm by combining Eqs. (3) and (6). Therefore, the

Table 2
Section geometric parameters of the SMPC-LL.

Parameters	t (mm)	R_1 (mm)	R_2 (mm)	d (mm)	L_s (mm)	L_o (mm)	ΔL (mm)
Value	1.50	4.38	4.38	5.00	27.50	37.50	10.00

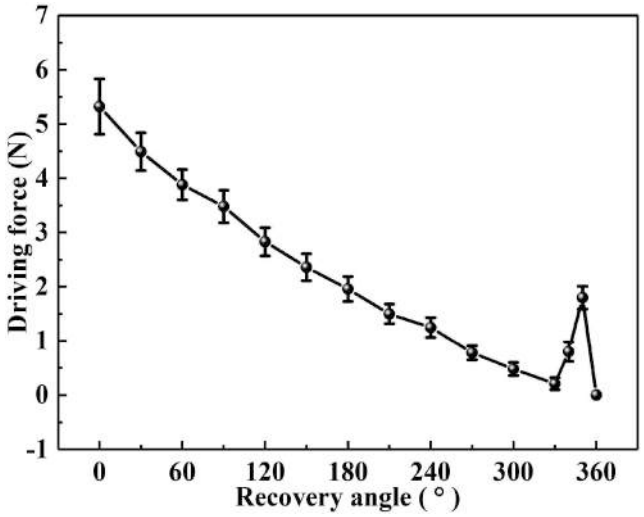

Fig. 3. Driving force of the SMPC-LT at different recovery angles.

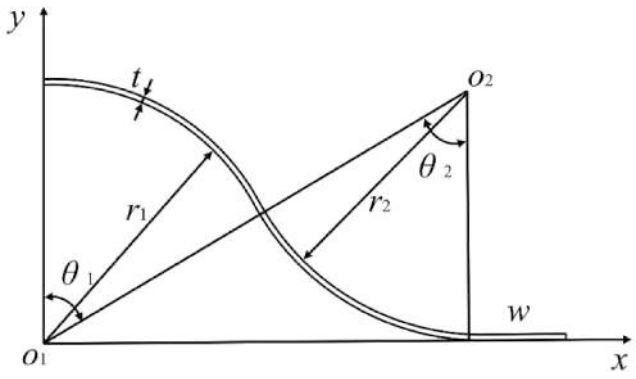

Fig. 4. 1/4 cross-sectional diagram of the SMPC-LT.

storage length and original length of the SMPC-LL could be determined by combining Eqs. (1) and (2). The section geometric parameters of the SMPC-LL are shown in Table 2.

Notably, the deployment function was mainly realized by the SMPC lenticular tubes (SMPC-LTs). The SMPC-LTs were curled into cylindrical shapes before deployment. As the ambient temperature gradually reached the T_g of the material, the SMPC-LTs began to recover to their original state, thereby achieving the deployment of SMPC-FSAS. Due to the high stiffness and excellent shape performance for lenticular shape, the SMPC-LT was selected in the system. Our previous study has demonstrated the performance of the SMPC-LT [24], and the structural dimension of the SMPC-LT have been carefully optimized [34]. Further, the driving force at the end of the SMPC-LT was tested. Due to the limitations of testing methods, only the SMPC-LT was curled 360° to test the driving force at different recovery angles. During the test, the heating film was pasted on both sides of the SMPC-LT to provide heat source. The power of a single heating film was 40 W. The test schematic diagram and test results are shown in Fig. 3. It can be observed that the maximum driving force of the SMPC-LT was about 5.32 N. When the recovery angle reached 330°, the driving force increased, which was

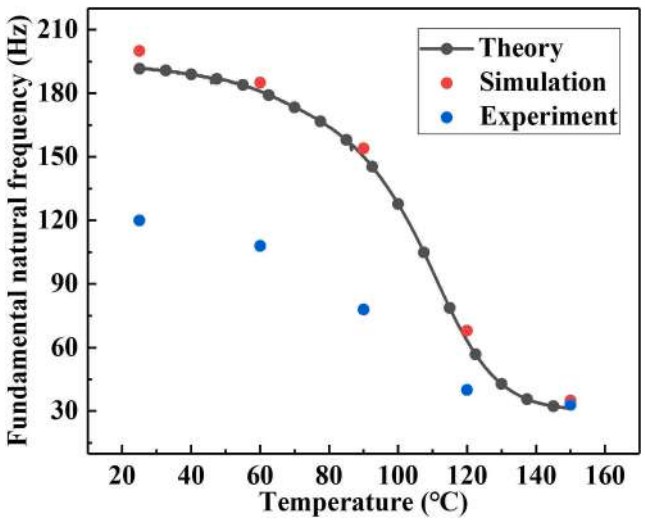

Fig. 5. Theoretical, simulation and experimental results of the relationship between fundamental natural frequency and surface temperature of the SMPC-LT.

caused by the bulging of the inner cavity of the SMPC-LT and the increase of the section stiffness.

In this study, the dynamic performance of the SMPC-LT was further studied. Fig. 4 shows a 1/4 cross-sectional diagram of the SMPC-LT. The area moment of inertia of the SMPC-LT can be expressed as follows:

$$I_x = 4\int_0^{\theta_1} tr_1(r_1 cos\theta)^2 d\theta + 4\int_0^{\theta_2} tr_2(r_2 - r_2 cos(\theta_2 - \theta))^2 d\theta + \frac{4wt^3}{3} \tag{7}$$

where I_x is the area moment of inertia to the X-axis, t is the thickness of the SMPC-LT, θ_1 and θ_2 are the central angles of the two arcs, r_1 and r_2 are the radii of the two arcs, and w is the length of the straight part on one side.

Where $\theta_1 = \theta_2 = 60°$, $r = r_1 = r_2 = 17$ mm, and $t = 0.4$ mm. Because the thickness of the SMPC-LT was very small, the contribution of the straight part to the area moment of inertia was negligible. Therefore, the expression of the area moment of inertia could be transformed into:

$$I_x = 4\int_0^{\frac{\pi}{3}} tr(rcos\theta)^2 d\theta + 4\int_0^{\frac{\pi}{3}} tr\left(r - rcos\left(\frac{\pi}{3} - \theta\right)\right)^2 d\theta = \left(\frac{8\pi}{3} - 3\sqrt{3}\right) r^3 t \tag{8}$$

Therefore, the natural frequency of the SMPC-LT can be expressed as [35]:

$$f = \frac{K_n}{2\pi}\sqrt{\frac{EI_x}{A\rho l^4}} \tag{9}$$

where A is the cross-sectional area of the SMPC-LT, ρ is the density of the SMPC-LT ($\rho = 1520$ kg/m^3), E is the elastic modulus, l is the length of the SMPC-LT, and K_n is a constant where n refers to the modal of vibration ($K_1 = 3.52$). Substituting Eq. (8) into Eq. (9) gives:

$$f = \frac{K_n r}{2\pi}\sqrt{\frac{\left(\frac{8\pi}{3} - 3\sqrt{3}\right)Ert}{A\rho l^4}} \tag{10}$$

According to Eq. (10), the fundamental natural frequency of the SMPC-LT could be designed by adjusting the geometric parameters. Fig. 5 illustrates the theoretical, simulation and experimental results of the relationship between the fundamental natural frequency and surface temperature of the SMPC-LT. The value of E in the theoretical and simulation calculations was obtained from the DMA curve previously studied [24]. The simulation results were basically consistent with the

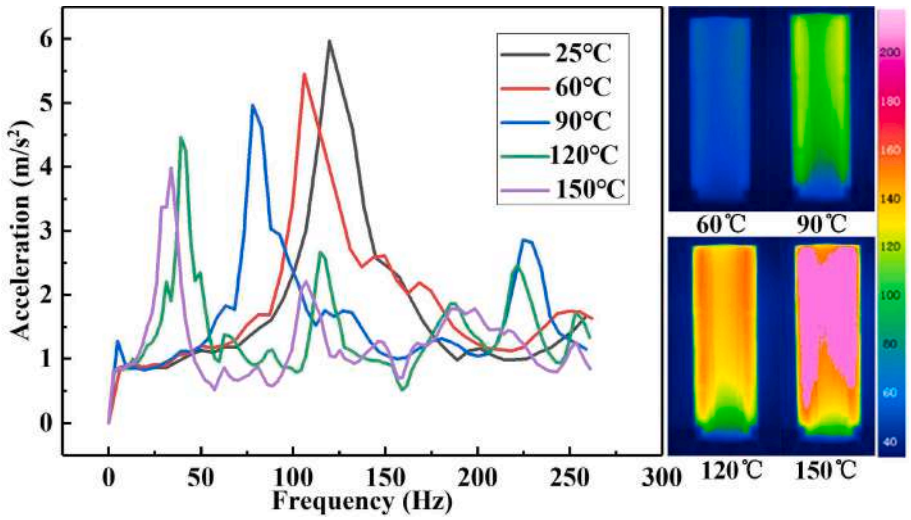

Fig. 6. Temperature distribution of the SMPC-LT.

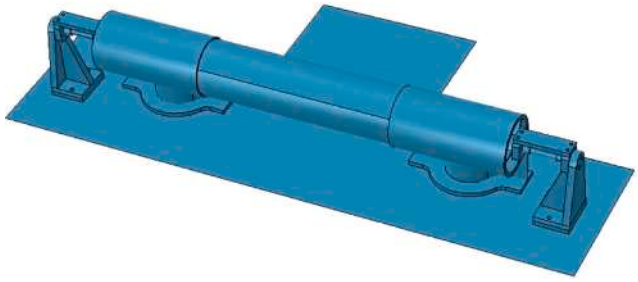

Fig. 7. Simplified numerical model of SMPC-FSAS.

Table 3
Material parameters of the titanium alloy and aluminum alloy.

Material	Density (Kg/m^3)	Modulus (GPa)	Poisson ratio	Allowable stress (MPa)
Titanium alloy	4500	110	0.30	860
Aluminum alloy	2700	72	0.33	266

Table 4
Material parameters of the unidirectional epoxy-based SMPC and cyanate-based SMPC.

Material	E_1 (GPa)	E_2 (GPa)	ν_{12}	G_{12} (GPa)	G_{13} (GPa)	G_{23} (GPa)
Epoxy-based SMPC	51.62	2.92	0.32	1.78	1.78	1.10
Cyanate-based SMPC	56.73	2.89	0.35	1.56	1.56	1.02

theoretical results, and both results were greater than the experimental results. The main reason is that the modulus obtained by DMA was larger than the real modulus [27], the fundamental natural frequency showed the same trend. In the experiment, the heating film provided the temperature environment, and the average temperature of the SMPC-LT was selected for the frequency sweep test. The frequency sweep curves and surface temperature distribution are shown in Fig. 6.

For the material selection of each component in the system, according to the dynamic environment assessment and the force transfer path analysis, it can be found that the stress on the locking mechanism was greater than that on other positions. Thus, a high strength titanium alloy was selected as the component of the locking mechanism. The cyanate-based SMP and epoxy-based SMP were used as the matrices of the SMPC-LL and SMPC-LT, respectively. Their glass transition temperatures were 203 ℃ and 150 ℃, respectively. The reinforcement phase of the two types of shape memory composite materials was carbon fiber twill, and the layup angle of the fiber was ±45°. The reason why the cyanate-based SMP with high T_g was selected as the matrix of the SMPC-LL was that the space thermal radiation environment was considered, and the cyanate-based SMP with high T_g could ensure that the SMPC-LL remained locking state in a complex space thermal environment. Different from the SMPC-LL, the epoxy-based SMP with low T_g was selected as the matrix of the SMPC-LT. This is because the two ends of the SMPC-LT were completely fixed, and the temperature environment had little effect on it. At the same time, the heating power required for low T_g materials was also very small. Aluminum alloy was selected as the material for other assembly parts.

3. Numerical simulation

3.1. Numerical model

Numerical simulation was performed to analyze the responses of the SMPC-FSAS under dynamic environments. The model was simplified during the structural modeling (as shown in Fig. 7). In the model, unsupported light shields and flexible solar array were removed. The base and SMPC-LTs were modeled with shell elements because they were thin-walled structures, and other parts were modeled with solid elements. The parts connected by bolts in the model were connected by tie, and the boundary condition base was fixed and loaded by the base. The parameters of the materials used in the SMPC-FSAS are shown in Table 3 and Table 4. The density and tensile strength of the epoxy-based SMPC were 1520 Kg/m^3 and 92 MPa, respectively, and the density and tensile strength of the cyanate-based SMPC were 1720 Kg/m^3 and 101 MPa.

3.1.1. Modal simulation

A numerical modal simulation of the four states was performed to analyse the modal of SMPC-FSAS. The first state was the entire structure in a stowed state to investigate the structural stiffness. The second state was the structure in a stowed state after removing the locking mechanism to understand the function of the locking mechanism. The third state was the structure in a stowed state after removing the SMPC-LTs to investigate the stiffness of the main frame. Finally, the fourth state was the entire structure in the deployed state, so that the stiffness of the

Table 5
The first four resonant frequencies in different states.

Structural state	Resonant frequency (Hz)			
	First-order	Second-order	Third-order	Fourth-order
First state	142.1	143.0	281.6	321.5
Second state	17.6	19.1	19.7	23.9
Third state	287.6	326.1	376.8	643.5
Fourth state	21.3	37.7	81.5	107.5

structure after deployment in orbit could be evaluated.

3.1.2. Swept sine vibration simulation

A numerical simulation of the swept sine vibration was conducted to observe the acceleration response and structural strength of the system and to provide a reference for subsequent swept sine vibration experiments. Based on obtaining structural modals, the structural characteristic swept sine vibration analysis was performed, and the frequency range was 5~100 Hz. The frequency range was 5~20 Hz, with a magnitude of 7.4 mm, while the frequency range was 20~100 Hz, with a magnitude of 12 g. The low-frequency part converts the amplitude into acceleration according to Eq. (11) and inputs the conditions according to the frequency acceleration amplitude.

$$A_a = (2\pi f)^2 A_u \tag{11}$$

where A_a represents acceleration, A_u represents amplitude, and f represents frequency.

3.2. Numerical analysis

3.2.1. Modal analysis

The first four resonant frequencies were obtained by a numerical modal analysis of different structural states (as shown in Table 5). By comparing the different structural states, it can be concluded that after the locking mechanism was added, the fundamental frequency of the structure was increased from 17.6 Hz to 137.8 Hz, which proved that the design of the locking mechanism could effectively improve the stiffness

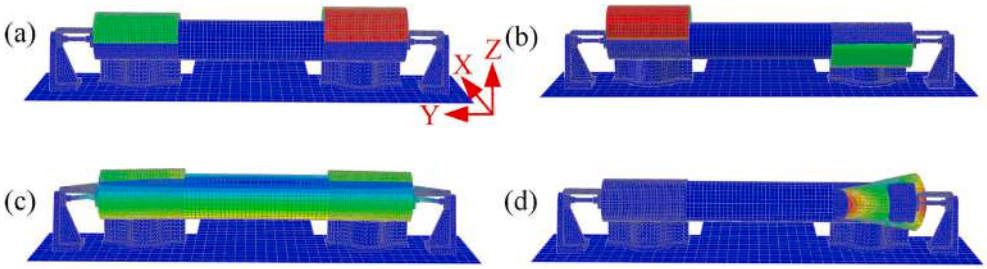

Fig. 8. The vibration modes of the SMPC-FSAS in the stowed state; (a) the first-order mode; (b) the second-order mode; (c) the third-order mode; (b) the fourth-order mode.

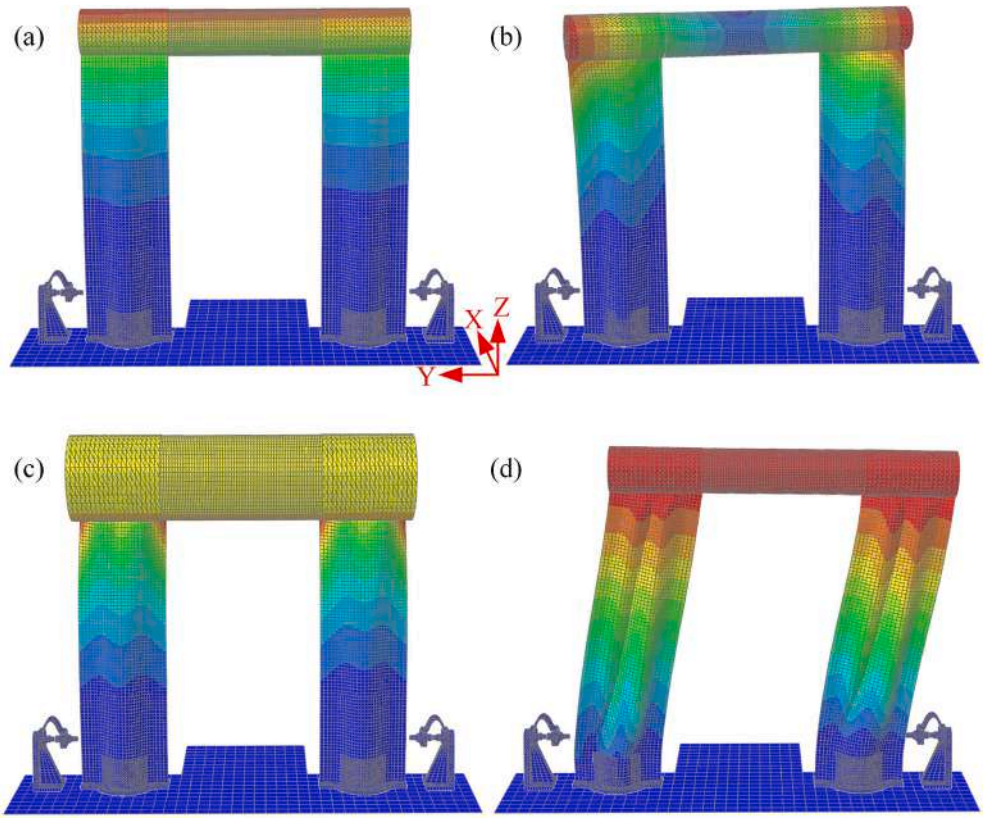

Fig. 9. The vibration modes of the SMPC-FSAS in the deployed state: (a) the first-order mode; (b) the second-order mode; (c) the third-order mode; (b) the fourth-order mode.

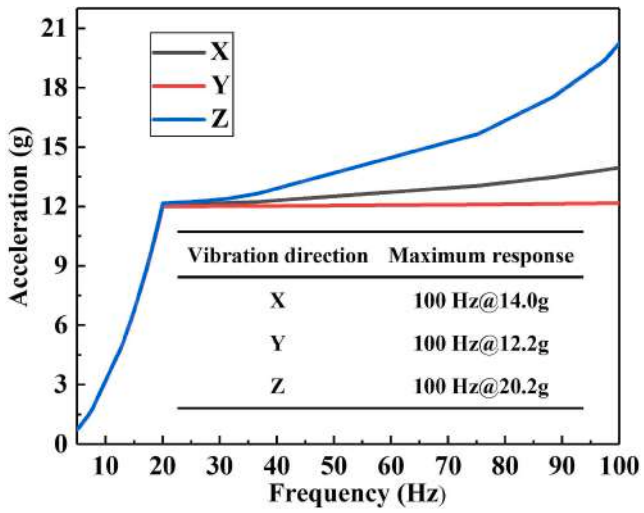

Fig. 10. Acceleration response of the swept sine vibration simulation in three orthogonal directions.

Table 6
Strength check of the swept sine vibration in three orthogonal directions.

Material	Maximum stress (MPa)			Safety margin
	X-direction	Y-direction	Z-direction	
Titanium alloy	10.1	88.3	55.0	8.7
Aluminum alloy	1.7	14.3	12.8	17.6
Epoxy-based composite	1.6	2.9	5.7	15
Cyanate-based composite	3.8	35.7	24.9	1.8

of the structure. When the SMPC-LTs were removed from the SMPC-FSAS, the fundamental frequency of the main structure was increased by 149.8 Hz compared with the entire structure. This is because before removing the SMPC-LTs, only two ends of the SMPC-LT in the curled state were fixed, while the SMPC-LT in the middle part was not fixed and flexible. Therefore, the structural flexibility was large. When the SMPC-LTs was removed, only the drum was rigidly locked by the locking mechanism, so the structural stiffness was large at this time. Therefore, after removing the SMPC-LTs, the fundamental frequency will get improved. However, due to the low mass of SMPC-LTs, so they had no great influence on the main structure under the dynamic environment.

Fig. 8 shows the modes of the SMPC-FSAS in the stowed state. The first four-order resonant frequencies of the SMPC-FSAS were 142.1 Hz (Z-component), 143.0 Hz (Z-component), 281.6 Hz (X-component), and 321.5 Hz (Y-component), respectively. The main vibration mode of the SMPC-FSAS corresponds to the swing of the SMPC-LTs. The modes of the SMPC-FSAS in the deployed state are shown in Fig. 9. The first four resonant frequencies of the SMPC-FSAS in the deployed state were 21.3 Hz (X-component), 37.7 Hz (Z-rotation), 81.5 Hz (X-component), and 107.5 Hz (Y-component), respectively. The main vibration mode was the swing of the SMPC-LTs and middle drum. The minimum mode of the SMPC-FSAS in the deployed state is mainly bending along the X-direction. This is because the moment of inertia of the SMPC-LT in the X-direction was relatively small.

3.2.2. *Swept sine vibration analysis*

During the test, an observation point was arranged on the SMPC-LT so that the acceleration response under swept sine vibration could be evaluated. Fig. 10 show the acceleration response on the SMPC-FSAS in three orthogonal directions. The acceleration response increased with the increase of loading frequency, and the maximum acceleration response in different vibration directions appeared at 100 Hz. This is because the resonant frequency of the SMPC-FSAS was 136.50 Hz, and the structure did not reach its resonant frequency. The maximum acceleration in the Z-direction was 20.2 g, which was 1.44 times and 1.65 times that in the X- and Y-directions, respectively. The stiffness of SMPC-FSAS in the Z-direction was the least in the stowed state. Table 6 presents the strength check of the swept sine vibration in three orthogonal directions. The safety margin of the SMPC-FSAS was calculated as Eq. (12). The SMPC-FSAS was not damaged during the vibration process, and the safety margins of the materials were all greater than 1.

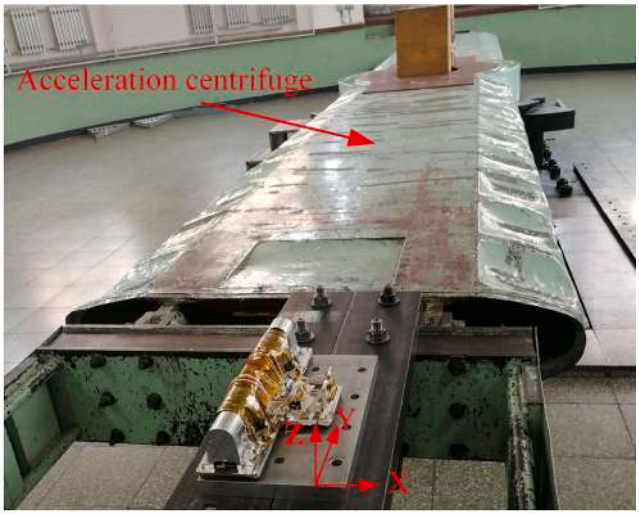

Fig. 12. Acceleration test of the SMPC-FSAS in the stowed state [33].

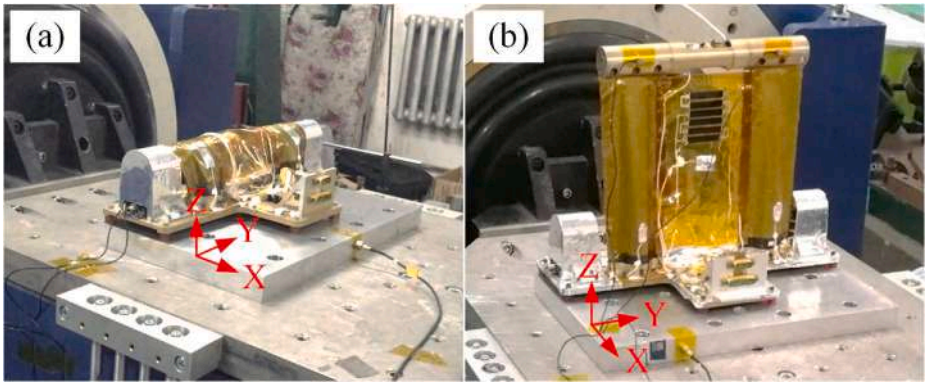

Fig. 11. Vibration test of the SMPC-FSAS: (a) stowed state; (b) deployed state [33].

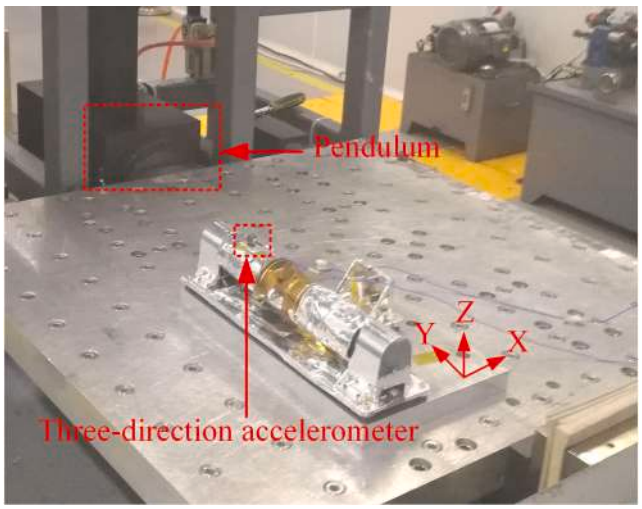

Fig. 13. Shock test of the SMPC-FSAS in the stowed state [33].

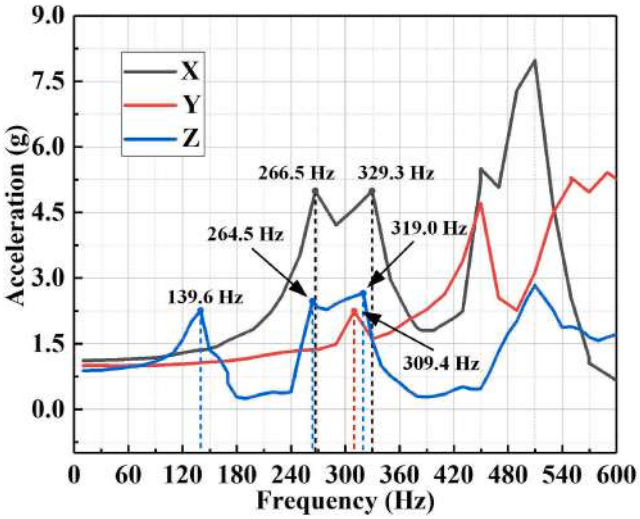

Fig. 14. Characteristic swept sine vibration of the SMPC-FSAS in the stowed state.

Table 7
Comparison between the simulation results and experimental results of the characteristic swept sine vibration in the stowed state.

	First-order	Second-order	Third-order	Fourth-order
Experiment (Hz)	139.6	–	265.0	309.4
Simulation (Hz)	142.1	143.0	281.6	321.5
Relative error (%)	1.8	–	6.3	4.0

$$MS = \frac{[\sigma]}{\sigma_{max}} - 1 \tag{12}$$

where MS denotes the safety margin, [σ] denotes the allowed stress of the material, and σ_{max} denotes the maximum stress.

4. Experiments

4.1. Vibration test

A swept sine vibration test was performed to examine the response of the SMPC-FSAS. Vibration tests of the SMPC-FSAS in the stowed and deployed states are shown in Fig. 11a and b, respectively. The results of the modal analysis in Section 3 revealed that the acceleration sensor adhered to the surface of the SMPC-LT. However, in the deployed state, the drum had a large displacement, so the acceleration sensor was placed on the drum. The input conditions of the swept sine vibration in the stowed state of the SMPC-FSAS were the same as those used in swept sine vibration simulation. As the SMPC-FSAS was not subjected to a harsh vibration environment after deployment, this study used a 0.2 g characteristic swept sine vibration to obtain the resonant frequency after deployment. The frequency range was from 5~1000 Hz, with a sweep rate of 4 oct/min.

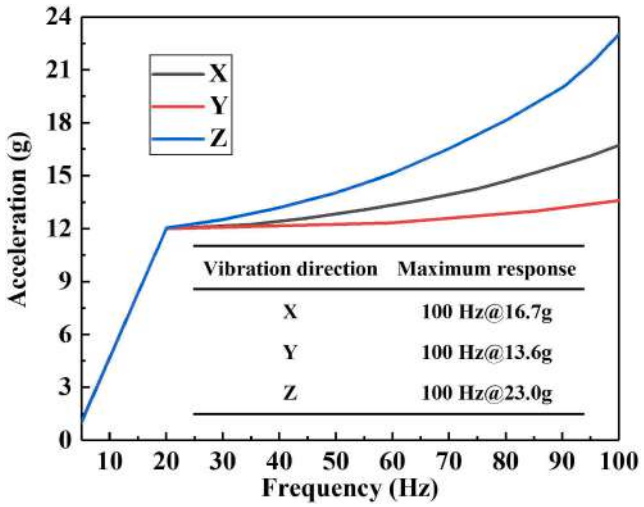

Fig. 15. The acceleration response of the swept sine vibration in the three orthogonal directions.

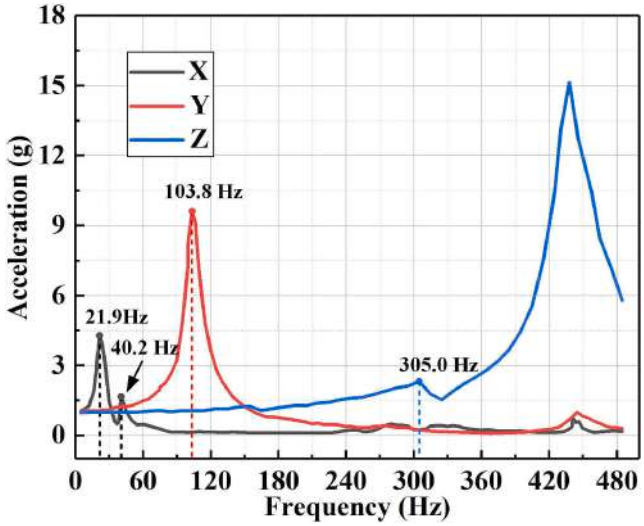

Fig. 16. Characteristic swept sine vibration of the SMPC-FSAS in the deployed state.

Table 8
Comparison between the simulation results and experimental results of the characteristic swept sine vibration in the deployed state.

	First-order	Second-order	Third-order	Fourth-order
Experiment (Hz)	21.9	40.2	–	103.8
Simulation (Hz)	21.3	37.7	81.5	107.5
Relative error (%)	2.7	6.2	–	3.5

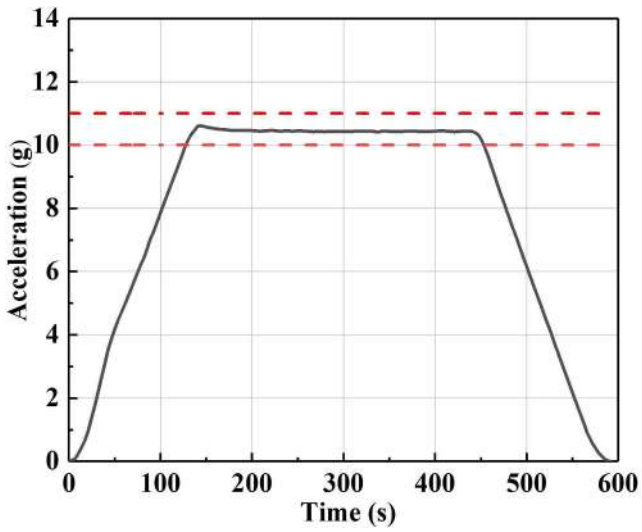

Fig. 17. Acceleration test curve of the SMPC-FSAS in the stowed state.

4.2. Acceleration test

Acceleration also affects the common dynamic environment of a spacecraft. A Type 43 acceleration centrifuge was used to generate centrifugal acceleration. The test process is shown in Fig. 12. During the test, the middle shaft rotated at a certain speed to provide different centripetal accelerations according to the specific required loading conditions. Acceleration tests were conducted in three orthogonal directions of the SMPC-FSAS, where the acceleration magnitude was 10 g for each direction, and the loading was carried out at a certain steady loading rate. After the magnitude of acceleration reached 10 g, the rotational loading was maintained for 5 min, and unloading was carried out at the same loading rate.

4.3. Shock test

The rocket launch process is inevitably subjected to shock loads. To understand the shock response of the SMPC-FSAS under a shock load, a shock test was performed using a CXP-100 shock-response spectrum testbed (as shown in Fig. 13), where the three-direction accelerometer was placed on the SMPC-LT. The shock test was also performed in three orthogonal directions. When the frequency range was 100~1500 Hz, the shock loading rate was +6 dB/oct. When the frequency range was 1500~4000 Hz, the shock magnitude was 1600 g.

5. Results and discussion

5.1. Vibration test analysis

Fig. 14 outlines the characteristic swept sine vibration in the three

Table 9
The maximum shock response of the SMPC-FSAS in the stowed state.

Shock loading direction	Maximum shock acceleration (g)			
	Control	X	Y	Z
X	2467	820	1296	916
Y	1966	2982	1261	3023
Z	3933	1179	496	2240

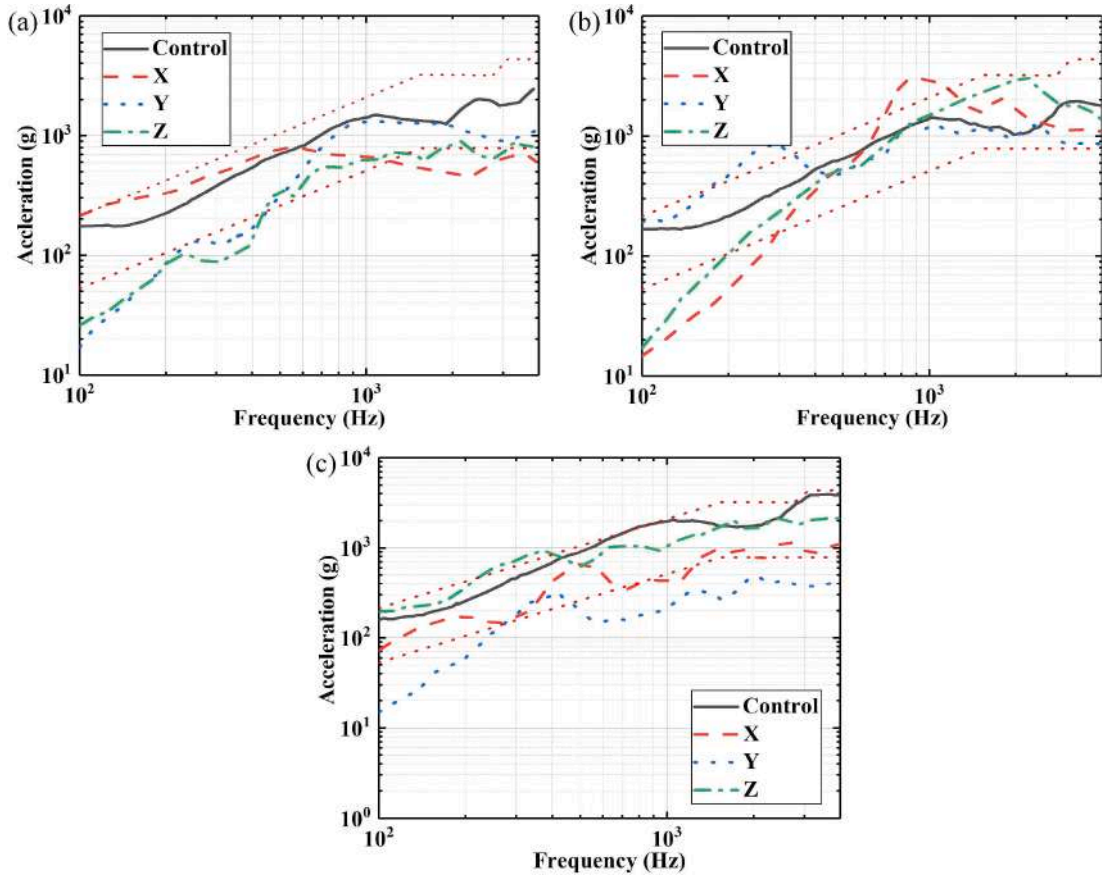

Fig. 18. The shock responses of the SMPC-FSAS in the stowed state: (a) acceleration responses under the X-direction shock; (b) acceleration responses under the Y-direction shock; (c) acceleration responses under the Z-direction shock.

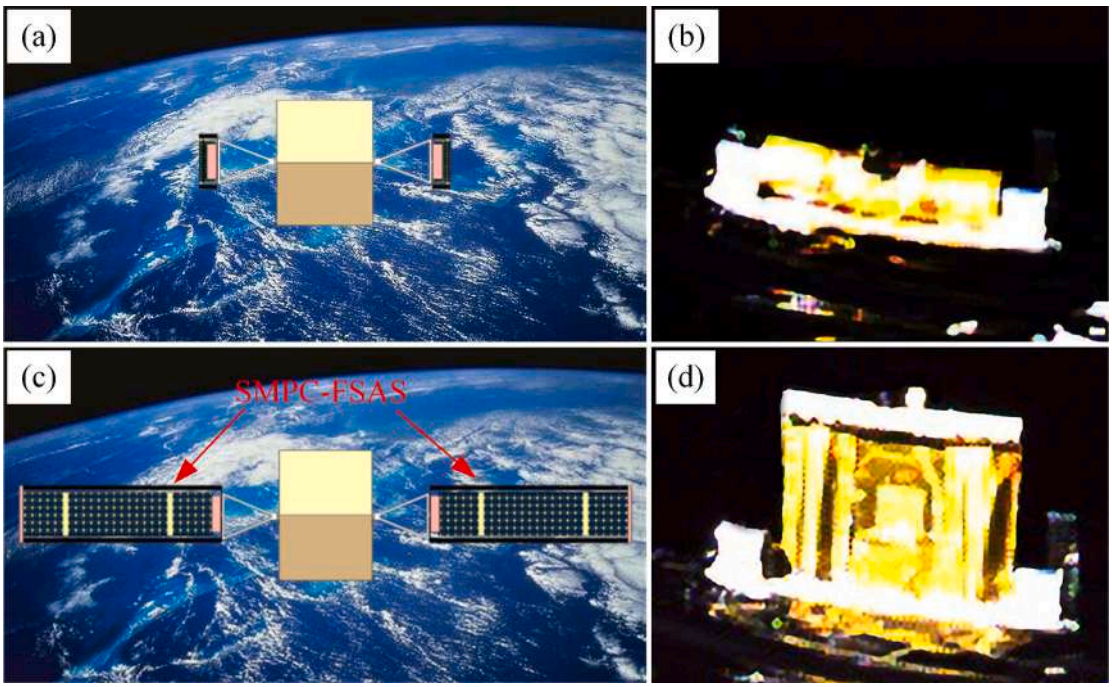

Fig. 19. On-orbit demonstration and application of the SMPC-FSAS: (a) stowed state of the ultra-large SMPC-FSAS; (b) on-orbit demonstration in the stowed state; (c) deployed state of the ultra-large SMPC-FSAS; (d) on-orbit demonstration in the deployed state [33].

orthogonal directions of the SMPC-FSAS in the stowed state. It can be perceived from the characteristic swept sine vibration results that the corresponding first-order resonant frequencies in the X-, Y-, and Z-directions were 266.5 Hz, 309.4 Hz, and 139.6 Hz, respectively. By averaging the resonant frequencies in the X-, Y-, and Z-directions, the first three order resonant frequencies of the SMPC-FSAS were 139.6 Hz, 265.0 Hz, and 309.4 Hz, respectively. Table 7 lists the simulation results and experimental results of the characteristic swept sine vibration of the SMPC-FSAS in the stowed state. The relative error of the first resonant frequencies was 1.8%, and the relative errors of the third-order and fourth-order resonant frequencies were 6.3% and 4.0%, respectively. Owing to the position of the acceleration sensor, the second-order resonance frequency in the numerical simulation was not collected. The experimental results were in good agreement with the results of the modal simulation. As the finite element model was simplified, the experiment had an acceptable error. Fig. 15 shows the swept sine vibration response of the SMPC-FSAS in the stowed state in the three orthogonal directions. It can also be observed from the figure that no resonant peak was found for the SMPC-LT in three orthogonal directions, which indicates that the SMPC-FSAS did not undergo resonance. When the vibration frequency reached 100 Hz, the maximum acceleration responses in the X-, Y-, and Z-directions were 16.7 g, 13.6 g, and 23.0 g, respectively. The results were in good agreement with the numerical results. Simultaneously, no damage was found on the surface of the SMPC-FSAS after all the tests were performed.

Fig. 16 presents the characteristic swept sine vibration of the SMPC-FSAS in the deployed state. From the results of the characteristic swept sine vibration, the corresponding first-order resonant frequencies in the X-, Y-, and Z-directions were 21.9 Hz, 103.8 Hz and 300.2 Hz, respectively. Combining the resonant frequencies in the three orthogonal directions, the first three resonant frequencies of the SMPC-FSAS were 21.9 Hz, 40.2 Hz, and 103.8 Hz, respectively. The peak value of the first-order acceleration response appears in the X-direction. This is because the stiffness of the SMPC-LTs in the X-direction was less than that in the other two directions. Table 8 shows the simulation and experimental results of the characteristic swept sine vibration of the SMPC-FSAS in the deployed state. The relative errors of the first two resonant frequencies were 2.7% and 6.2%, respectively, and the relative error of the fourth-order resonant frequency was 3.5%. The test results were in good agreement with the simulation results. In addition, the resonant response direction of the characteristic swept sine vibration was consistent with that of the simulation results.

5.2. Acceleration test analysis

The acceleration test curve of the SMPC-FSAS in the stowed state is shown in Fig. 17. It can be seen from the figure that the rate of loading and unloading was about 0.08 g/s, the maximum acceleration was 10.6 g, with a maximum time of 15 s, an average acceleration of 10.5 g, and a constant speed time of 300.1 s, which met the experimental requirements. During the experiment, the structure did not show any abnormalities.

5.3. Shock test analysis

Fig. 18a-c plots the acceleration responses under shock loads in three orthogonal directions. The shock control curves in the three directions were within the effective range, proving the effectiveness of the shock test. The maximum responses of the SMPC-FSAS in the stowed state are listed in Table 9. The maximum acceleration values under shock loads in the X-, Y- and Z-directions were 1296 g, 3023 g and 2240 g, respectively. Furthermore, the structural stiffness in the Z-direction was smaller than that in the X- and Y-directions, and the result was consistent with the swept sine vibration result.

6. Application

At present, the solar array widely used by small satellites has the disadvantages of low deployment to storage ratio and low power-to-weight ratio, which restricts the development of small satellites. Flexible solar arrays based on SMPCs are light weight and high storage ratio, so they have potential application prospects in the field of small satellites. In this study, the SMPC-FSAS carried on the SJ-20 geostationary satellite was launched into the geosynchronous orbit on December 27,

2019 and a controlled deployment in the orbit was achieved. Fig. 19 shows the on-orbit demonstration and application of the SMPC-FSAS. In the stowed state, the system can be stowed into a smaller volume (as shown in Fig. 19a). The system is deployed through the shape memory properties of the material itself, and the deployed state is shown in Fig. 19c. Fig. 19b and 19d show the deployment of the SMPC-FSAS in orbit. It can be shown that the SMPC-LT achieved nearly 100% deployment, and drove the deployment of the flexible solar array. It is also promising for use in space stations and space solar power stations. Accordingly, the results of this study, particularly the successful deployment of the SMPC-FSAS provides new insights into the deployment technology of space solar arrays.

7. Conclusions

In this work, the structural and dynamic analysis of the SMPC-FSAS was investigated. In the structure of the SMPC-FSAS, epoxy-based SMP and cyanate-based SMP were used as the matrices of the SMPC-LT and SMPC-LL respectively. The locking mechanism and deployment mechanism based on SMPC were designed to guarantee the safety and reliability of the structure under dynamic environments. By comparing the fundamental frequencies of structures in different states, it was proved that the locking mechanism could effectively improve structural stiffness. The modal simulation results indicated that the minimum resonant frequencies in the stowed and deployed states were 142.1 Hz and 21.3 Hz respectively, which was consistent with the experimental results. Furthermore, the strength and rigidity of the SMPC-FSAS were validated using 12 g swept sine vibration, 1600 g shock and 10 g acceleration tests. In particular, the successful launch and controlled deployment of the SMPC-FSAS on a geosynchronous orbit for the first time in the world have fully demonstrated the safety and reliability of SMPC-FSAS. In the future, a large-scale flexible solar array system will be developed based on the SMPC-FSAS, which will make a significant contribution to spacecraft power generation systems.

Declaration of Competing Interest

The authors declare that they have no known competing financial interests or personal relationships that could have appeared to influence the work reported in this paper.

Acknowledgements

The authors would like to thank for the direction and help from Institute of Telecommunication Satellite, China Academy of Space Technology (CAST). The authors would like to also thank for the support from Shanghai Space Power Institute who has specially developed the flexible solar array for the SMPC-FSAS project. This work is supported by the National Natural Science Foundation of China (Grant No. 11632005, 11872020).

References

[1] Segiet D, Raidt T, Özdem H, Weckes S, Tiller JC, Katzenberg F. Thermo-/moisture-responsive shape-memory effect of poly (2-ethyl-2-oxazoline) networks. J Polym Sci Part B: Polym Phys 2019;57(16):1053–61.
[2] Leng J, Lv H, Liu Y, Du S. Electroactivate shape-memory polymer filled with nanocarbon particles and short carbon fibers. Appl Phys Lett 2007;91(14):144105.
[3] Tan L, Hu J, Ying Rena K, Zhu Y, Liu P. Quick water-responsive shape memory hybrids with cellulose nanofibers. J Polym Sci, Part A: Polym Chem 2017;55(4):767–75.
[4] Zhang D, Cheng Z, Liu Y. Smart wetting control on shape memory polymer surfaces. Chem Eur J 2019;25(16):3979–92.
[5] Roth PJ, Lowe AB. Stimulus-responsive polymers. Polym Chem 2017;8(1):10–1.
[6] Meng H, Li G. A review of stimuli-responsive shape memory polymer composites. Polymer 2013;54(9):2199–221.
[7] Herath M, Epaarachchi J, Islam M, Fang L, Leng J. Light activated shape memory polymers and composites: a review. Eur Polym J 2020;136:109912.
[8] Hu J, Zhu Y, Huang H, Lu J. Recent advances in shape–memory polymers: structure, mechanism, functionality, modeling and applications. Prog Polym Sci 2012;37(12):1720–63.
[9] Yu K, Xie T, Leng J, Ding Y, Qi HJ. Mechanisms of multi-shape memory effects and associated energy release in shape memory polymers. Soft Matter 2012;8(20):5687–95.
[10] Huang J, Zhang Q, Scarpa F, Liu Y, Leng J. Shape memory polymer-based hybrid honeycomb structures with zero Poisson's ratio and variable stiffness. Compos Struct 2017;179:437–43.
[11] Du H, Liu L, Zhang F, Leng J, Liu Y. Triple-shape memory effect in a styrene-based shape memory polymer: characterization, theory and application. Compos B Eng 2019;173:106905.
[12] Wang K, Strandman S, Zhu XX. A mini review: Shape memory polymers for biomedical applications. Front Chem Sci Eng 2017;11(2):143–53.
[13] Liu Y, Du H, Liu L, Leng J. Shape memory polymers and their composites in aerospace applications: a review. Smart Mater Struct 2014;23(2):023001.
[14] Pilate F, Toncheva A, Dubois P, Raquez J-M. Shape-memory polymers for multiple applications in the materials world. Eur Polym J 2016;80:268–94.
[15] Mu T, Liu L, Lan X, Liu Y, Leng J. Shape memory polymers for composites. Compos Sci Technol 2018;160:169–98.
[16] Gong X, Liu L, Scarpa F, Leng J, Liu Y. Variable stiffness corrugated composite structure with shape memory polymer for morphing skin applications. Smart Mater Struct 2017;26(3):035052.
[17] Lu H, Yu K, Sun S, Liu Y, Leng J. Mechanical and shape-memory behavior of shape-memory polymer composites with hybrid fillers. Polym Int 2010;59(6):766–71.
[18] Yu K, Liu Y, Liu Y, Peng H-X, Leng J. Mechanical and shape recovery properties of shape memory polymer composite embedded with cup-stacked carbon nanotubes. J Intell Mater Syst Struct 2014;25(10):1264–75.
[19] Ni Q-Q, Zhang C-S, Fu Y, Dai G, Kimura T. Shape memory effect and mechanical properties of carbon nanotube/shape memory polymer nanocomposites. Compos Struct 2007;81(2):176–84.
[20] Guo J, Wang Z, Tong L, Liang W. Effects of short carbon fibres and nanoparticles on mechanical, thermal and shape memory properties of SMP hybrid nanocomposites. Compos B Eng 2016;90:152–9.
[21] Afful HQ, Ibekwe S, Mensah P, Li G. Influence of uniaxial compression on the shape memory behavior of vitrimer composite embedded with tension-programmed unidirectional shape memory polymer fibers. J Appl Polym Sci 2020;138(20):50400.
[22] Santo L, Quadrini F, Bellisario D, Iorio L. Applications of shape-memory polymers, and their blends and composites. In: Shape Memory Polymers, Blends and Composites; 2020. p. 311–29.
[23] Santo L, Quadrini F, Accettura A, Villadei W. Shape memory composites for self-deployable structures in aerospace applications. Procedia Eng 2014;88:42–7.
[24] Liu Z, Li Q, Bian W, Lan X, Liu Y, Leng J. Preliminary test and analysis of an ultralight lenticular tube based on shape memory polymer composites. Compos Struct 2019;223:110936.
[25] Le VL, Le VT, Goo NS. Deployment performance of shape memory polymer composite hinges at low temperature. J Intell Mater Syst Struct 2019;30(17):2625–38.
[26] Tiwari N, Shaikh AA. Buckling and vibration analysis of shape memory laminated composite beams under axially heterogeneous in-plane loads in the glass transition temperature region. Appl Sci 2021;3:451.
[27] Liu Z, Lan X, Bian W, Liu L, Li Q, Liu Y, et al. Design, material properties and performances of a smart hinge based on shape memory polymer composites. Compos B Eng 2020;193:108056.
[28] Francis W, Lake M, Mallick K, Freebury G, Maji A. Development and testing of a hinge/actuator using elastic memory composites. In: 44th AIAA/ASME/ASCE/AHS/ASC structures, structural dynamics, and materials conference; 2003. p. 1496.
[29] Arzberger SC, Tupper ML, Lake MS, Barrett R, Mallick K, Hazelton C, et al. Elastic memory composites (EMC) for deployable industrial and commercial applications. In: Smart structures and materials 2005: industrial and commercial applications of smart structures technologies: International Society for Optics and Photonics; 2005. p. 35–47.
[30] Aoki T, Higuchi K, Watanabe K. Progress report of SIMPLE space experiment project on ISS Japan experiment module. T Jpn Soc Aeronaut S 2014;12(ists29):Tc_1–6.
[31] Liu T, Liu L, Yu M, Li Q, Zeng C, Lan X, et al. Integrative hinge based on shape memory polymer composites: Material, design, properties and application. Compos Struct 2018;206:164–76.
[32] Li F, Liu L, Du L, Liu Y, Leng J. Mechanical analysis of a tip-loaded deployable truss based on shape memory polymer composite. Compos Struct 2020;242:112196.
[33] Lan X, Liu L, Zhang F, Liu Z, Wang L, Li Q, et al. World's first spaceflight on-orbit demonstration of a flexible solar array system based on shape memory polymer composites. Sci China Technol Sc 2020;63(8):1436–51.
[34] Chu Z, Lei Y. Design theory and dynamic analysis of a deployable boom. Mech Mach Theory 2014;71:126–41.
[35] Young WC, Budynas RG, Sadegh AM. Roark's formulas for stress and strain. McGraw-Hill Education; 2012.